Functionality and Activity of Sol−Gel-Prepared Co and Fe co-Doped Lead-Free BTO for Thermo-Optical Applications

Mohammed Tihtih, Jamal Eldin F. M. Ibrahim,* Mohamed A. Basyooni, Redouane En-nadir, Irina Hussainova, and István Kocserha

Read Online

ACCESS | Metrics & More | Article Recommendations

ABSTRACT: The BTO, BFTC, and BCTF compounds were synthesized by the sol−gel method. The XRD study revealed the formation of single-phase tetragonal perovskite structures with the space group (P4mm). The crystalline parameters were studied as a function of Fe and Co contents and occupation of Ba and/or Ti sites by Fe and Co in the BTO lattice. It was found that the obtained strain increases when Ba^{2+} is substituted by Co^{2+} and Ti^{4+} by Fe^{3+}. The Raman investigation confirmed the existence of three active modes (B1/E (TO1LO), (E (TO)/A1(TO3), and (A 1(LO)/E (TO)), all of which are related to the existence of the tetragonal phase and strongly support the XRD results. The microstructural study showed a clear correlation between the presence of Fe and Co and the grain size distribution. Optical studies revealed the improvement in band gap energy with transition-metal (Fe and Co) co-doped BTO ceramics. The decrease in the band gap is explained by the competing effects of Columbian interactions, microdeformation, and oxygen defects. The results indicate that the presence of Fe and Co dopants enhances the absorption in the BTO ceramic. The dopants demonstrated an effect on thermal conductivity: they decreased the thermal conductivity of BTO, which is in the range of 0.76−2.23 W m^{-1} K^{-1} at room temperature and 2.02−0.27 W m^{-1} K^{-1} at elevated temperatures. The microstructure of the manufactured materials and the grain size distribution affect the compressive strength.
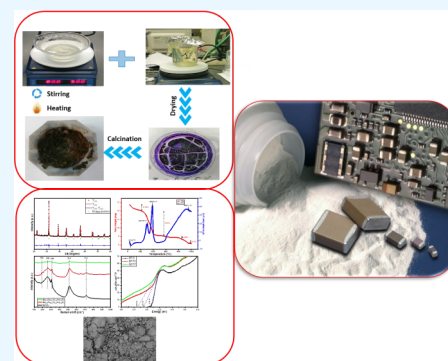
1. INTRODUCTION

Ceramic compounds play an important role in the electronic industry due to their high dielectric constant and offer a wide range of applications, including actuators, sensors, power transmission, capacitors, and high-energy storage devices.[1−4] However, most high dielectric constant ceramics, such as PZT (lead zirconium titanate ceramics), contain lead which is hazardous to both humans and the environment.[5,6] To replace lead-based ceramics, more environmentally friendly materials have been explored. BaTiO$_3$ is one of the well-known lead-free ceramic materials with a wide range of applications in optoelectronics: thermistors, capacitors, piezoelectric devices, positive temperature coefficient of resistance (PTCR), and semiconductors.[7−10] BaTiO$_3$ (BTO) has the formula of a typical perovskite structure ABO$_3$, where Ba is the A site and Ti is the B site. The structural, thermal, and optical properties can be improved by suitable ion doping or co-doping. The structure, microstructure, optical property, and thermal conductivity behavior of BTO ceramics can be improved by doping a cation at the A site or B site. In general, the site occupancy of a dopant can be predicted based on its ionic radius. For example, a dopant with a large ionic radius and low valence will be more likely to occupy the A site of the Ba^{2+} ion (rBa^{2+} = 1.35), and a dopant with a small ionic radius and high

valence will be more likely to occupy the B site of the Ti^{4+} ion (rTi^{4+} = 0.61 Å).[9]

In the last decades, extensive research has been carried out to synthesize a doped BTO material with controlled particle size distribution and high purity. As a result, numerous techniques have been used to prepare pure and doped BTO materials, including the sol−gel method,[11,12] autocombustion route,[13] solid-state reaction,[14] and hydrothermal reaction,[15] to enhance its structural, electrical, optical, thermal, and mechanical properties.[4] Among all these methods, sol−gel is considered an effective technique that allows the production of materials with high purity at the nanoscale, better control of stoichiometry, minimum particle agglomeration, homogeneity at a microscopic level, reduction in the sintering temperature, and more uniform powders.[16]

Recently, modified BTO materials have attracted special attention because they exhibit favorable structural, optical, and
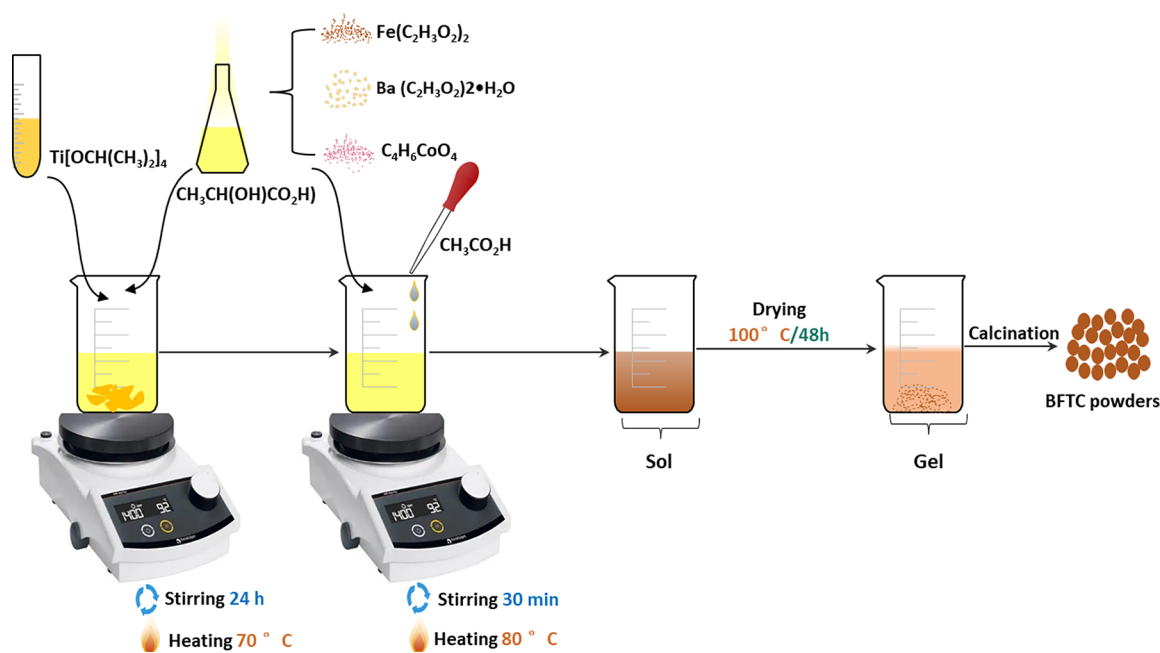
Figure 1. Flowchart of the preparation of BCTF samples by the sol−gel method.

electrical properties at low temperatures.[17,18] BTO is a promising multifunctional material that can be doped with transition metal ions such as Fe, Ni, Co, and so forth or other impurities for a variety of applications.[19−21] Typically, a ferroelectric substance can acquire the ferromagnetic property by injecting transition-metal dopants into the ferroelectric system material.[22,23] Moreover, pure BTO exhibits lower ionic conductivity and behaves as an insulator at room temperature. According to the defect model, the substitution of double acceptor impurities in titanates at Ti sites and in barium at Ba sites improves both the ionic and electronic conductivities accompanied by the formation of charge carriers and oxygen vacancies. The dominant charge carriers depend on the synthesis conditions and on the concentration of unintentional acceptor/donor impurities. The most considerable increase in thermal and electrical conductivities is achieved by Fe and Co substitutions. The common valences of Fe and Co are known to be 3+ and 2+. Both the Fe and Co ions can be substituted in the BTO lattice. Understanding the effect of both Fe and Co substitutions on the structural, microstructural, and various physical properties would be a major step to the clarification of these properties for use in optoelectronic applications.[24]

The structural, electrical, and magnetic properties of Fe- and Co-doped BTO were reported in refs 25−27. McCracken and co-workers have investigated Fe and Co transition-metal-doped BTO and their effects on the major properties of BTO.[28] It has been shown that the straightforward solvothermal synthesis is suitable for the rational design of Co- and Fe-doped BTO materials with a sufficient degree of control over the size, shape, and internal structure of the nanocrystals. To the best of our knowledge, there is no comparative research on Fe^{3+} and Co^{2+} co-doped BTO perovskites; therefore, an additional study is needed. The lead-free Fe- and Co-modified BTO ceramics are promising materials for pyroelectric energy conversion to create self-powered and "battery-less" devices.[29,30] Similarly, the evaluation of the optical property is essential as it is considered one of the most important properties of BTO ceramics, which is

required for the development of the optical band gap to determine the Urbach energy and other parameters such as the metallization criterion of the photocatalyst and so on. Co- and Fe co-doped BTO ceramics is a candidate material for achieving high catalytic activity, material stability, and oxygen permeability in various atmospheres at high temperatures. The doping of 3d to 5d transition-metal atoms at both Ba sites and Ti sites in $BaTiO_3$ with a relatively large band leads to electronic and ionic conductivities, usually attributed to hopping conduction along the Ti−O−Ti bonding.[31] The small polaron hopping conductivity is apparently influenced considerably by a carrier formation mechanism due to the variation of the valence state (or redox state) of both the matrix and dopant cation and the electronegativity of TiO_6 octahedron.[32] Further, Fe is usually used as a dopant in the industrial fabrication of MLCCs because it shows similar properties and is less expensive. Co and Fe co-doping improves the insulation resistance, results in high conductivity and permittivity, and inhibits the growth of dielectric grains, dielectric loss, and high leakage current used in manufacturing MLCCs.[33] It also enhances the temperature stability of BTO, changes the lattice parameters, shifts the Curie temperature, enhances the band gap energy, and reduces the sinterability of BTO as both Fe and Co elements conserve a high melting point.[34]

Thermal conductivity is an important parameter for assessing the durability and integrity of electronic applications, as it is one of the most fundamental thermal transport properties that are critical for thermal management.[35] Also, for a better understanding of internal stress-affected multilayer ceramic capacitors (MLCCs), the study of mechanical properties such as Young's modulus and compressive strength of co-doped BTO ceramic samples is crucial for improving the eternity and the reliability of MLCCs.[36] Numerous studies have been carried out to produce and investigate modified BTO with various substitutes such as Fe and Co at Ba and/or Ti sites[37,38] to improve its fundamental properties.[39−41] Recently, Fe^{3+}- and Co^{2+}-doped BTO materials have attracted
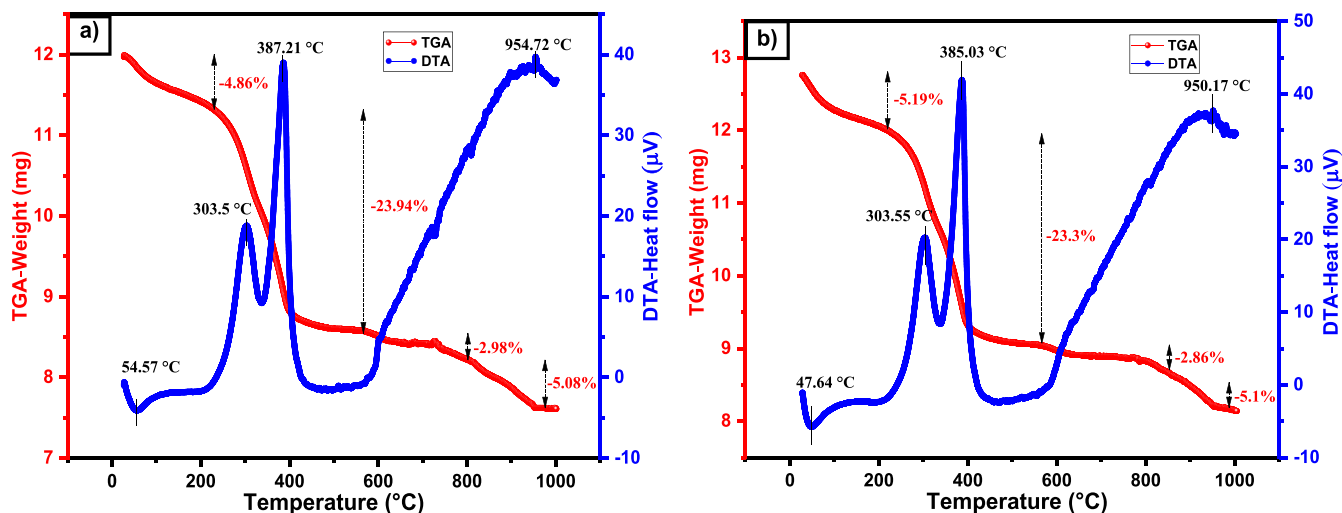
Figure 2. TGA and DTA graphs of the raw ceramic powders (a) BFTC and (b) BCTF.

great interest as important technological lead-free ceramic materials.[34,42,43] However, to the best of our knowledge, no similar studies have been performed to investigate the optical behavior and thermal conductivity as a function of temperature as well as the compressive strength of sol−gel-produced Co and Fe co-doped BTO.

In this study, $BaTiO_3$ (BTO), $(Ba_{0.97}Fe_{0.03})(Ti_{0.97}Co_{0.03})O_3$ (BFTC), and $(Ba_{0.97}Co_{0.03})(Ti_{0.97}Fe_{0.03})O_3$ (BCTF) ceramics were prepared by the sol−gel method. DTA/TGA and XRD analyses were performed to demonstrate the thermal and structural properties of the fabricated samples. Raman spectroscopy was used to identify the vibrational energy modes of the manufactured BTO, BFTC, and BCTF powders. FTIR spectra were used to confirm the vibrational groups present in the synthesized samples. In addition, the role of Co and Fe incorporation at A and B sites in the lead-free BTO ceramic compounds is described in detail using structural analysis. Scanning electron microscopy (SEM) was performed to identify the morphology, homogeneity, and size distribution of the studied samples. The optical behavior and band gap of the synthesized samples were studied by UV−vis spectroscopy. The thermal conductivity of the ceramic compounds was measured as a function of temperature. Detailed analyses of the compressive strength of BTO, BFTC, and BCTF were also investigated.

2. EXPERIMENTAL SECTION

2.1. Synthesis. The BTO, BFTC, and BCTF samples were synthesized using the wet chemical sol−gel reaction technique. The high-purity products of barium acetate Ba $(C_2H_3O_2)_2$-H_2O, iron acetate $Fe(C_2H_3O_2)_2$, cobalt(II) acetate $C_4H_6CoO_4$, and titanium alkoxide $Ti[OCH (CH_3)_2]_4$ were used as raw materials. Acetic acid CH_3CO_2H was used to aid the rapid solubility of the acetates, and distilled water H_2O was used as a solvent. Figure 1 shows different processes for the synthesis of BTO, BFTC, and BCTF ceramic materials (example of a BFTC ceramic material). The first process involves the preparation of a clear TiO_2 solution. To prepare 150 mL of TiO_2 solution, 36 g of titanium alkoxide, 5.6 g of lactic acid, and 75 g of distilled water are required. A continuous stirring for 24 h with 300 rpm speed at 70 °C produces a combination that gradually changes into a transparent sol. In a second process, the resulting colloidal transparent solution was added

stoichiometrically to the acetates of barium, iron, and cobalt. After drying at 80 °C and milling, the gel was then converted into fine particles. Finally, the fine powders produced were calcined at 980 °C for 3 h in a programmable furnace at a heating rate of 5 °C/min.

2.2. Characterization. Thermogravimetric and differential thermal analyses were performed using a Netzsch STA 409 PC Luxx thermal analyzer in the range from room temperature to 1000 °C. An X-ray diffractometer (XPERT-PRO) with Cu−Kα radiation (λ = 1.54059 Å) was used to study the structural behavior of the synthesized powders. The vibrational groups present in the synthesized samples were identified using a Bruker-Tensor 27 spectrophotometer. A Senterra dispersive Raman microscope was also used to study at room temperature the phase present in the synthesized samples over the scan range of (90−950 cm^{-1}) at an excitation wavelength of 785 nm. To accomplish a good sinterability of the prepared compounds, the ceramics were formed into pellets by applying 7 tons/cm^2 of uniaxial pressure. The samples were then heated at 1200 °C for 6 h. The morphology and microstructure of the fracture surface of the ceramic pellets were visualized using a scanning electron microscope, Carl Zeiss EVO MA10, controlled at 20 kV. A combination of the standard thermal conductivity meter (TCi C-Therm) and the modified transient plane source (MTPS) method was used to determine the variation in thermal conductivity. The compressive strength values were determined using a universal electronic testing machine (WDW-50). An Ocean Optics QE65Pro UV−vis spectrophotometer with diffuse reflectance was used to record the UV−vis spectrum. Finally, the compressive strength at fracture under a loading rate of 1 mm min^{-1} was recorded in MPa.

3. RESULTS AND DISCUSSION

3.1. Thermal Analysis. Figure 2 displays the thermal degradation curves of BFTC and BCTF xerogels. The raw powders were subjected to thermal decomposition at the temperature range of 22−1000 °C in air with a heating rate of 5 °C/min. The thermal analysis reveals that the total weight loss is approximately 37%, divided into four stages of decomposition, which are seen in the TGA curves. At about 22−231 °C, the initial mass loss (about 4% for BFTC and 5% for BCTF) was detected, corresponding to an endothermic
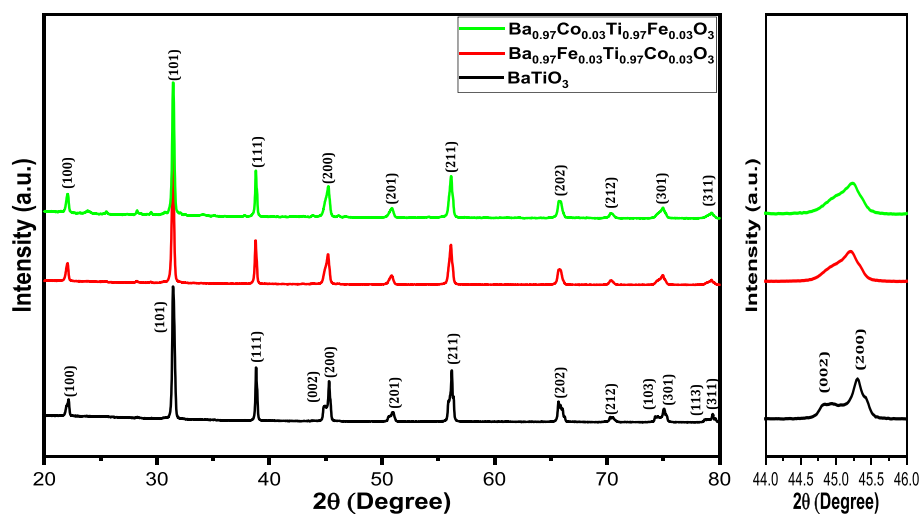
Figure 3. XRD patterns of BTO, BFTC, and BCTF ceramic powders.

process caused by the evaporation of surplus water and lactic acid. In the second step of mass loss, where the important mass loss was detected, the TGA spectrum indicated that the weight of BFTC and BCTF dropped by about 23.9 and 23.3%, respectively. The decomposition of the organic Ba−Ti materials and the distortion of the gel structure could be the causes of the weight loss at this stage.[11,44] The DTA curves showed two peaks at about 303−387 °C caused by the evaporation of organic chemical residues and the decomposition of acetates contained in the samples. The carbonate phases (intermediate phases) are assumed to have formed in the third stage, which show a weight loss of 2.98% (557−798 °C) and 2.86% (564−852 °C) for BFTC and BCTF, respectively. Finally, the observed weight loss between 798 and 960 °C (about 5%) and 852−960 °C (5%) is due to the crystallization of the BFTC and BCTF ceramic samples. The completion of the polymorphic transformation process of the samples is indicated by the exothermic peaks at 954 and 950 °C in the DTA curves which are directly related to the decomposition of the carbonate phase. This study has shown that the crystallization of the current ceramic samples occurs at a temperature of about 980 °C.

3.2. Crystalline Structure. The X-ray diffraction patterns of BTO, BFTC, and BCTF ceramics are shown in Figure 3. The X-ray diffraction patterns of BTO, BFTC, and BCTF are consistent with the tetragonal structure and *P4mm* space group. Table 1 shows the lattice parameters obtained from the analysis of the XRD data using the Rietveld refinement method. The lattice parameters of BTO are in good agreement with the values reported in the literature and with our recently published results.[4,12,45,46] Table 1 shows that the lattice constant a remains almost constant with the Fe and Co doping elements, while the lattice constant c decreases, which is due to the incorporation of Fe^{3+} and Co^{2+} into the sites of Ba^{2+} (1.35 Å) and Ti^{4+} (0.60 Å), which is directly due to the difference in the ionic radius of the presented ions (Fe^{3+}, Co^{2+}, Ba^{2+}, and Ti^{4+}). Further, the c/a ratio of the tetragonal lattice system decreased from 1.010 (BTO) to 1.005 for BCTF. The obtained lattice parameters of Co- and Fe-doped BTO are in good agreement with the values reported in the literature for single Fe-doped BTO nanoparticles.[47] This can be seen as a result of the influence of dopants, which allows them to achieve the same properties as in wet chemical methods such

as sol−gel and hydrothermal methods or even ball-milled BTO. A similar comparison can be made between the deviation of the c/a ratio and the values reported in the literature when Co^{2+} is present in the Ti site.[48] Masó et al.[49] have found that the c/a tetragonality of Fe-doped BTO decreases on the Ti-site side, while the dopant content increases. The decrease in tetragonality (c/a ratio) as a function of Fe and Co doping is strong evidence for the tetragonal differential type of the samples. This is confirmed by the separation of the (0 0 2) level plane in BFTC and BCTF, which occurs in BTO in addition to the (2 0 0) level plane (Figure 3).

The crystal structure of any given system depends on the ionization states and coordination number of its constituents. In BTO, Ti^{4+} and Ba^{2+} have coordination numbers of 6 and 12, respectively. In co-doped compounds, in both cases, Ba site and Ti site, Ba^{2+} is substituted by Fe^{3+} and/or Co^{2+}, which carry the same coordination number, and Ti^{4+} is also replaced by Fe^{3+} and/or Co^{2+}, depending on the doping reactants, so that Fe can have a coordination number of 6. Therefore, the contraction of the unit cell will occur.[50] At a certain point, the incorporation of Fe into the Ba/Ti site should distort the lattice system and consequently produce a microstrain. The Williamson−Hall method is used to quantitatively validate the resulting microstrain. Using this technique, the distinct contributions of instrumental broadening, crystallite size, and lattice strain can be resolved. Nonetheless, with respect to doping, we are more interested in lattice contraction or expansion. The Scherrer and Wilson formulas were used to determine the crystallite size and strain parameters, respectively, and the estimated results are given in Table 1

$$\beta\cos\theta = \frac{0.9\lambda}{D} + 4\varepsilon\sin\theta \qquad (1)$$

$$D = 0.9\lambda/\beta\cos\theta \qquad (2)$$

where D is the crystallite size, λ is the Cu Kα wavelength, θ is the peak position, β is the full width at half-maximum, and ε is the strain. Due to the variation of unit cell volume shrinkage, the calculated strain increases by 2.13 when Co^{2+} is incorporated into Ba^{2+} and Fe^{3+} into Ti^{4+}. The calculated strain for BTO was 1.27, which agrees well with the value reported by Rajan et al.[51] BCTF and BFTC are in the range of

Table 1. Physical and Crystallographic Parameters of BTO, BFTC, and BCTF Ceramic Samples Using the Rietveld Refinement Method

	BTO	BFTC	BCTF
a (Å)	3.9988	3.989	3.999
c (Å)	4.0398	4.0295	4.0192
c/a (Å)	1.010253	1.010153	1.005076
volume ($Å^3$)	64.59802	64.11789	64.27665
structure	tetragonal	tetragonal	tetragonal
space group	$P4mm$	$P4mm$	$P4mm$
x (Ba)	0		
y (Ba)	0		
z (Ba)	0		
x (Ba, Fe)		0	
y (Ba, Fe)		0	
z (Ba, Fe)		0	
x (Ba, Co)			0
y (Ba, Co)			0
z (Ba, Co)			0
x (Ti)	0.5		
y (Ti)	0.5		
z (Ti)	0.48347		
x (Ti, Fe)			
y (Ti, Fe)			0.5
z (Ti, Fe)			0.5
x (Ti, Co)		0.5	0.53387
y (Ti, Co)		0.5	
z (Ti, Co)		0.47384	
x (O1)	0.5	0.5	0.5
y (O1)	0.5	0.5	0.5
z (O1)	0.05854	0.03436	0.01600
x (O2)	0.5	0.5	0.5
y (O2)	0	0	0
z (O2)	0.51642	0.52693	0.54170
R_{Bragg}	5.027	7.02	7.89
R_p	17.3	22.8	23.4
R_{wp}	26.5	31.2	33
R_{exp}	22.15	41.01	38.7
χ^2	1.43	0.81	0.80
crystallite size (nm) (D)	30.14602	26.68294	22.69694
strain (ϵ)	1.27	1.32	2.13
density (g/cm^3)	6.02	6.001	5.891
tolerance factor (t)	1.07	1.058	1.063

a stable perovskite structure, although Fe and Co doping causes structural distortions in the lattice system. The stabilization of the presented compounds was confirmed by Goldschmidt's tolerance factor t (eq 3). The stability and structural distortions of the BFTC and BCTF perovskite structures are described by Goldschmidt's tolerance factor equation (t):[52]

$$t_1 = \frac{(0.97R_{Ba} + 0.03R_{Fe} + R_O)}{\sqrt{2}(0.97R_{Ti} + 0.3R_{Co} + R_O)} \quad (3)$$

$$t_2 = \frac{(0.97R_{Ba} + 0.03R_{Co} + R_O)}{\sqrt{2}(0.97R_{Ti} + 0.3R_{Fe} + R_O)} \quad (4)$$

where t_1 and t_2 represent the tolerance factor for BFTC and BCFT, respectively; R_{Ba}, R_{Co}, R_{Ti}, and R_{Fe} are the ionic radii of Ba^{2+}, CO^{2+}, Ti^{4+}, and Fe^{3+}; and R_O depicts the ionic radius of O^{2-} ion in the ferroelectric material $BaTiO_3$. An ideal cubic

perovskite structure has a tolerance factor of $t = 1$. The tolerance factor values in the currently examined samples range from 1.058 to 1.07, supporting the distortion in the tetragonal structure of perovskite ferroelectrics. Table 1 lists the tolerance factor (t) values for all compositions. The obtained results indicated that Co^{2+} and Fe^{3+} ions were successfully doped into Ba^{2+} and Ti^{4+} in a BTO lattice.

In a $BaTiO_3$ structure, the Ti and Ba ions are surrounded by 6 and 12 oxygen ions, respectively. Consequently, the incorporation of Fe^{3+} or Co^{2+} ions into Ti^{4+} ions leads to the shrinkage of the volume of the unit cell (V), and oxygen vacancies are created to correct the charge imbalance in the system. Based on the valence state of the dopant elements, three cases can be considered:

(i) Due to the different ionic radii of Ba^{2+}, Ti^{4+}, Fe^{3+}, and Co^{2+} ions, oxygen vacancies in the acceptor dopants corrected the charge imbalance.[53,54]

(ii) Donor dopants with higher ionic charges. In this case, Ba and/or Ti vacancies ($4Ba^{2+} + Ti^{4+} \rightarrow 4Ti^{3+} + V_{Ti}$; $3Ba^{2+} \rightarrow 2Ti^{3+} + V_{Ba}$) are generated to keep the balance of charges.

(iii) The variation of lattice parameters a and c, especially the decrease in parameter c of BFTC and BCTF ceramic samples, can be explained by oxygen vacancy formation along the C axis.[55]

Structural refinement using the Fullprof program was performed to estimate the crystallographic data and the various physical properties of the BTO, BFTC, and BCTF samples. To assess the quality of the structural refinement, R values are commonly utilized (R_{exp}, R_{Bragg}, R_{wp}, R_p, R_F, and χ^2).[56] In Rietveld refinement, four reliability parameters, namely, weighted profile (Rwp), profile residual (Rp), expected value ($Rexp$), and goodness-of-fit index (χ_I^2), are needed to be minimized, which are defined as[57]

$$R_{wp} = \left[\left(\sum_i w_i (I_{io} - I_{ic})^2 \right) \Big/ \left(\sum_i w_i I_{io}^2 \right) \right]^{1/2} \quad (5)$$

$$R_p = \frac{\sum_i |I_{io} - I_{ic}|}{\sum_i I_{io}} \quad (6)$$

$$R_{exp} = \left[(N - P) \Big/ \left(\sum_i w_i I_{io}^2 \right) \right]^{1/2} \quad (7)$$

$$\chi_I^2 = [R_{wp}/R_{exp}]^2 \quad (8)$$

where I_{io} and I_{ic} are the experimental and calculated intensities for the diffraction angle $2\theta_i$, and $w_i = (1/\sigma_i^2)$, σ_i being the standard deviation associated with the intensity at each $2\theta_i$ value. N and P are the weight and number of experimental observations and number of fitting parameters, respectively. The refinement was done using the space group $P4mm$, and convergence was achieved. The analysis of the peak profile has been performed by the pseudo-Voigt function. The calculated values of R_{exp}, R_{Bragg}, R_{wp}, R_p, R_F, and χ_I^2 after refinement are presented in Table 1. Figure 4 shows the experimental and fitted XRD patterns for all the presently studied compositions. The XRD data and Rietveld refinement of all compositions show the existence of a tetragonal, single-phase perovskite structure. Various refinement parameters, including lattice constants, confirmed that the BTO, BFTC, and BCTF compositions exhibit tetragonal symmetry.
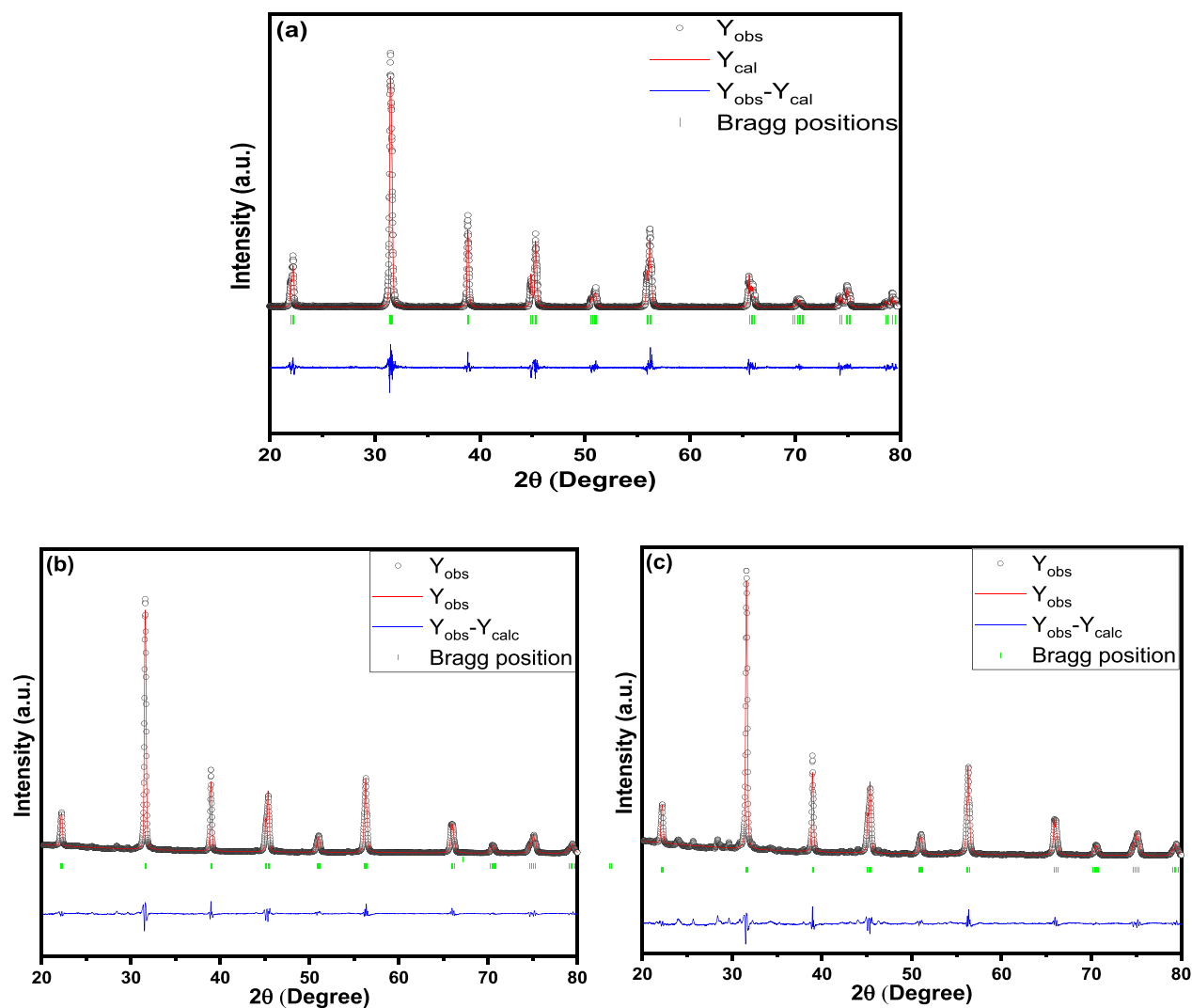
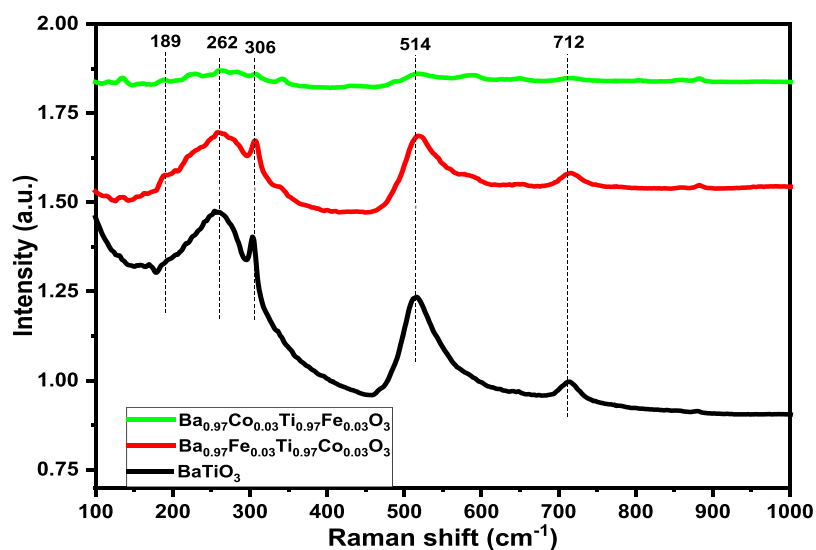**Figure 4.** Structural refinement of (a) BTO, (b) BFTC, and (c) BCTF ceramic powders using the Rietveld method.

Figure 5. Raman spectra of BTO-, BFTC-, and BCTF-produced samples.

3.3. Raman Investigation. Because of the strong connection between ferroelectricity and lattice dynamics, Raman spectroscopy is observed to be an effective method

to identify the vibrational energy modes in ferroelectric materials. ABO_3 perovskite materials have 15° of freedom above the cubic−tetragonal phase transition, which can be
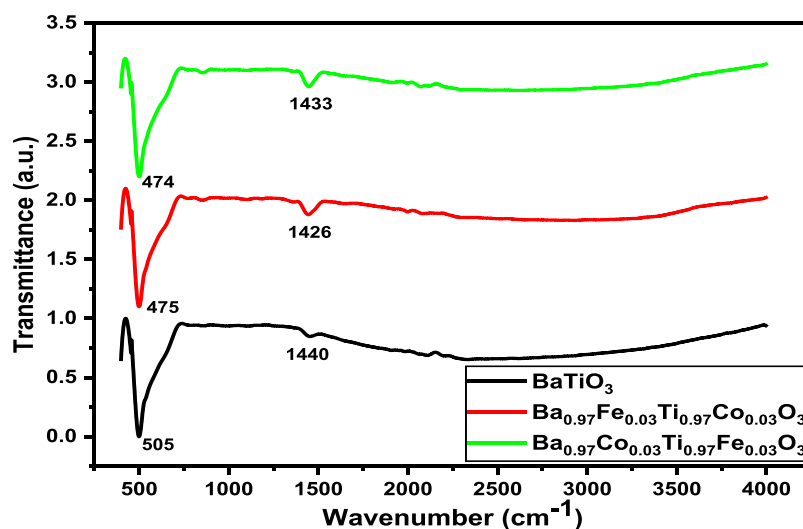
Figure 6. FTIR spectra of the prepared ceramic samples.

divided into 4F1u and 1F2u.[58] In this research work, the predicted structural phase in Co and Fe co-doped BTO samples was examined using Raman spectroscopy, through the observation of rotational, vibrational, and other low-frequency modes in the system of the presented ceramic samples. Figure 5 displays the Raman spectra of BTO, BFTC, and BCTF samples recorded at room temperature. According to the reported research results, the Raman modes detected in the Raman spectra of the tetragonal BTO single crystal (*P4mm*) are about 165 cm^{-1} [$A_1(TO_1)$], 266 cm^{-1} [$A_1(TO_2)$], 306 cm^{-1} [B_1, E(LO, TO)], 516 cm^{-1} [$A_1(TO_3)$], and 720 cm^{-1} [$A_1(LO_3)$, E(LO)] modes.[51,59] Theoretically, there are no active Raman modes in the cubic phase, confirming the existence of a single tetragonal phase. Raman analysis shows broad bands at around 251 and 520 cm^{-1}, possibly due to the local disorder associated with the position of the titanium atoms.[60] Moreover, all the observed Raman peaks in Figure 5 are associated with the tetragonal phase of the BTO, BFTC, and BCTF ceramic samples. Consequently, the active Raman modes (B_1/E (TO$_1$LO), (E (TO)/A_1(TO$_3$)), and (A_1(LO)/E (TO) situated at 262, 306, 514, and 712 cm^{-1}, respectively, are associated with the presence of a tetragonal single phase, which is in good agreement with the above XRD results.

3.4. FTIR Behavior. Figure 6 shows the FTIR spectra of the BTO, BFTC, and BCTF powders. The absorption peak at 854 cm^{-1} is due to the low-intensity dimension in the Ti−OR bond vibration, turning it into a single band and indicating the removal of the alkoxide groups. Due to the low content of BaCO$_3$ in the ceramic samples, the characteristic absorption in the range from 1433 to 1440 cm^{-1} is attributed to the stretching vibrations of carboxylate.[61] The distinctive Ti−O peak was shifted to lower energy values by the substitution of Fe and Co in the BTO lattice, and the bond distance of Ti^{4+} and O^{2-} ions was changed by the substitution of Co^{2+} and Fe^{3+} ions in Ba^{2+} and Ti^{4+} sites, resulting in a high bond strength.[62,63] Moreover, we can always detect a single absorption band at about 505, 475, and 474 cm^{-1} for BTO, BFTC, and BCTF, respectively, which can be attributed to the bending vibrations and stretching of the Ti−O bond in the [TiO$_6$]$^{2-}$ octahedron.[64] Thus, there is a good agreement between the obtained FTIR results and Raman and X-ray diffraction analyses.

3.5. SEM Analysis. Figure 7 displays illustrations of the SEM images and grain size distribution of BTO, BFTC, and BCTF pellets sintered at 1200 °C for 6 h. The manufactured ceramic samples are uniformly dense and composed of flat block grains with randomly oriented grains. This can be explained by the fact that the particle system tends to expand into larger particles to reduce the total surface free energy.[65−67] The average grain size (AGS) of the BTO, BFTC, and BCTF ceramics was determined by fitting the Gaussian distribution from ImageJ software, and the values are listed in Table 2. The average grain size decreased after doping from approximately 8.7 μm for BTO to 5.9 μm for the BCTF ceramic sample. However, the average grain size values for the sintered pellets are larger than those theoretically calculated from the crystallite sizes; the observed difference is attributed to the sintering parameters improving the mechanical strength of the samples. The co-doped samples with 3% Fe and 3% Co exhibit a homogeneous microstructure and are relatively small-grained compared to the BTO samples where Fe and/or Co are incorporated into Ba and Ti sites, leading to the formation of defect complexes (e.g., 2Co$_{Ba}$ − Fe$_{Ti''}$). Yb and Sm co-doped BTO with charge compensation exhibited a small-grained microstructure and homogeneous distribution, as reported by Jo et al.[68] SEM results showed that Fe and Co substitutions in the BTO ceramic material were necessary for optimal microstructure evolution.

3.6. Optical Behavior and Band Gap Energy. UV−vis spectroscopy is used to study the optical absorption in a given material. In ceramic perovskite materials, there is a very fine relationship between the crystalline structure and the physical properties. Small structural changes can lead to significant changes in physical behavior. The Kubelka−Munk function[69] was used to express the absorption results by applying the following equation;

$$\alpha(\lambda) = F(R) = \frac{(1-R)^2}{2R} = \frac{k}{S} \tag{9}$$

where *K* is the absorption coefficient, *R* is diffuse reflectance, *S* is the scattering coefficient, and $\alpha(\lambda) = F(R)$ is the Kubelka−Munk function (proportional to the absorbance coefficient) developed by Munk and Kubelka.[69] The interband transition type was examined using the $F(R)$ function and the McLean
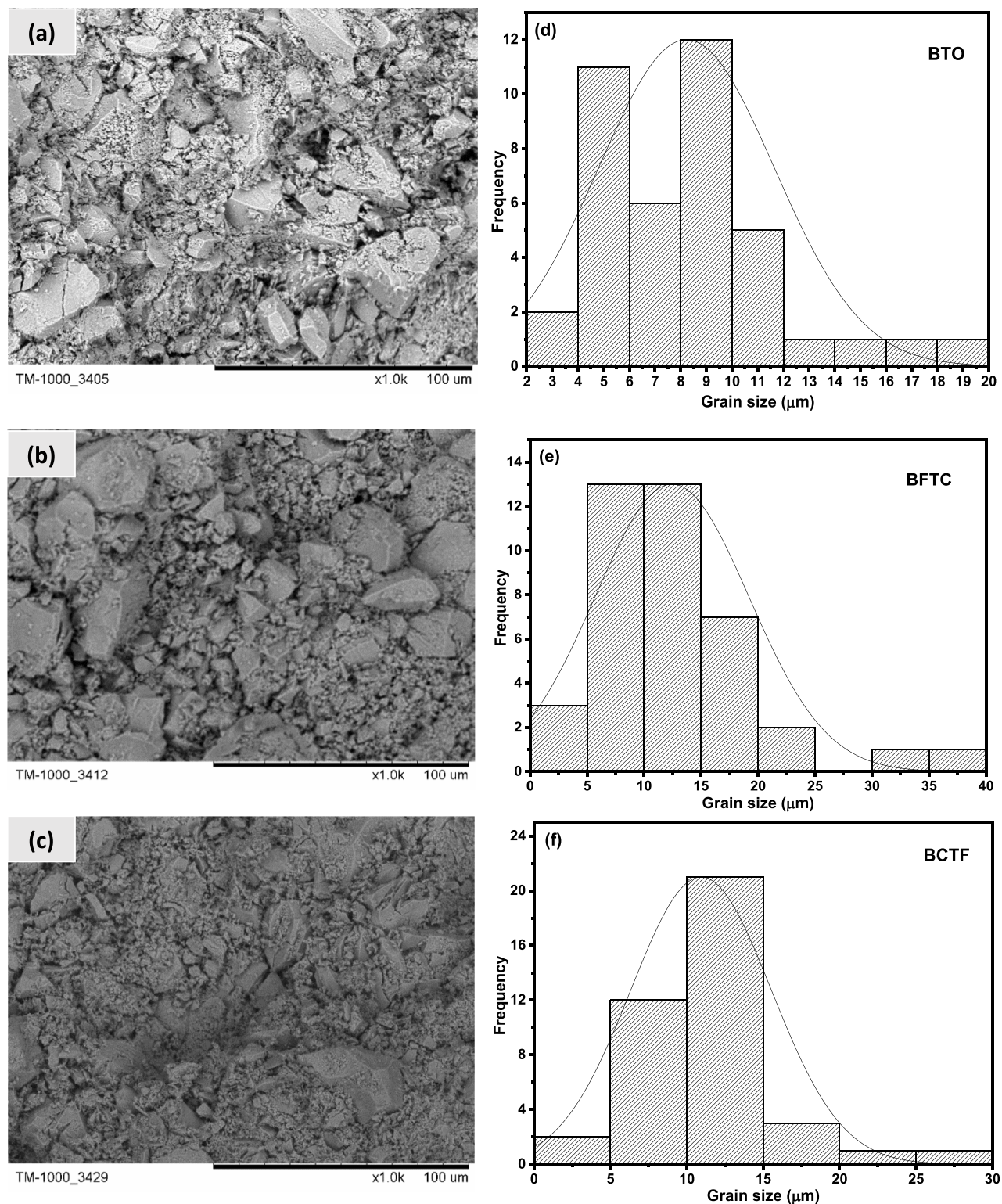
Figure 7. (a−c) SEM images. Grain size distribution of (d) $BaTiO_3$, (e) $(Ba_{0.97}Fe_{0.03})(Ti0_{.97}Co_{0.03})O_3$, and (f) $(Ba_{0.97}Co_{0.03})(Ti_{0.97}Fe_{0.03})O_3$.

Table 2. Average Grain Size of the Samples

sample	average grain size (AGS) (μm)
BTO	8.7
BFTC	6.1
BCTF	5.9

method. The Tauc plot method can be used to estimate the optical band gap (E_g) using the following equation

$$\alpha h\nu = C_1(h\nu - E_{gap})^n \tag{10}$$

$F(R) \equiv \alpha(\lambda) = K/S$, ν, C_1, and h parameters are presented, respectively, as the absorption coefficient, light frequency, proportionality constant described as the band tailing parameter, and Planck's constant. Index n can have different
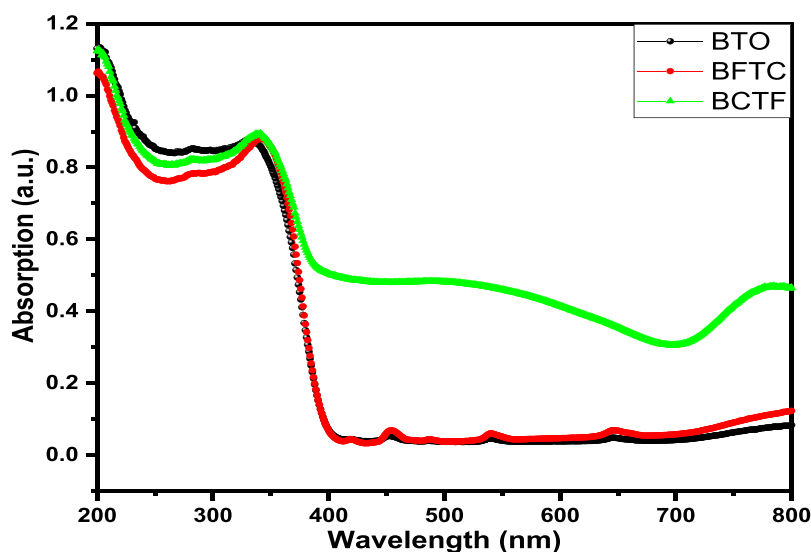
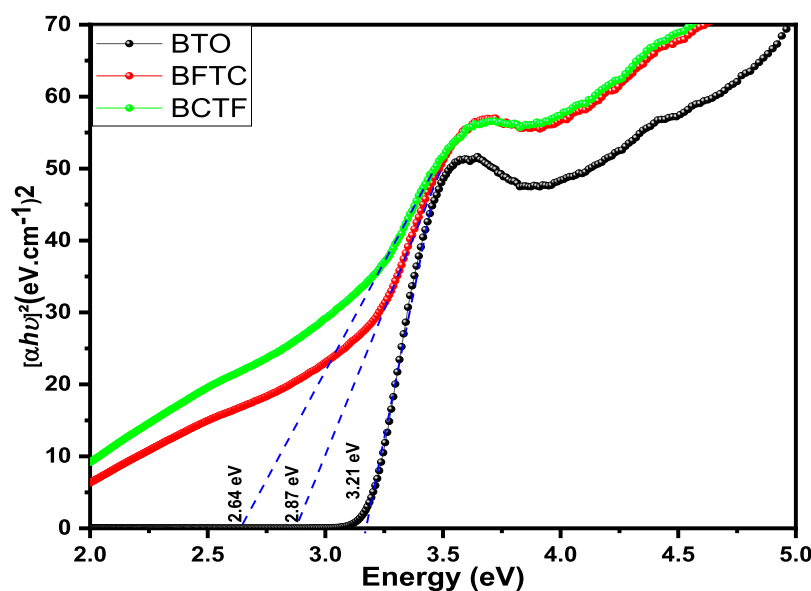**Figure 8.** UV−vis spectrum of BTO, BFTC, and BCTF samples.

Figure 9. Optical band gap energy of the ceramic materials.

possible values: it is equal to 1/2 for direct allowed, 2 for indirect allowed, 3/2 for direct forbidden, and 3 for indirect forbidden transitions. The optical band gap value is obtained from eq 10 by extrapolating the tangential line from a high photon energy.

Figure 8 shows the absorption spectra of the studied ceramic materials; the samples exhibit significant UV absorption in the range from 275 to 523 nm. The observed peaks, particularly in the visible region, show that the samples exhibit strong visible light absorption, which makes them function as interesting photocatalyst materials. Figure 8 also illustrates how the BTO absorption peak extends into the visible region and how new absorptions appear between 450 and 540 nm. The absorption changes from BTO to BCTF samples and shifts to the visible region between 375 and 545 nm. As a result, new absorption peaks are identified between 455 and 540 nm. The decrease in absorption intensity for the BFTC and BCTF compositions could be attributed to the increase in conductivity due to the Fe and Co substitutions.[70] Based on our findings and reference

to the observed absorption spectra, it is indicated that the charge-transfer pathways between the O2p nonbonding level and the 3° orbital were eliminated as a result of the coexistence of Ti^{4+} along Fe^{3+} and Co^{2+}. Therefore, spin-forbidden transitions are induced in the samples, which can be explained by the significant enhancement of the charge-transfer mechanisms along $(O^{2+}-Fe^{3+})$ and $(O^{2+}-Co^{2+})$.

Figure 9 shows the band gap energies of the ceramic samples BTO, BFTC, and BCTF calculated by the Tauc plot method. It was found that the wide band gap for the BTO sample is 3.21 eV, which is close to the band gap values reported in the literature,[71] while the band gap energies for BFTC and BCTF are 2.87 and 2.64 eV, respectively. The significant decrease in the optical band gap energy from 3.21 eV to 2.64 for BCTF can be interpreted by the occurrence of distortions within the octahedral Ti−O rearrangement of the molecular orbitals.[72] In addition, the variation in particle size could be the reason for the decrease in the band gap energy.[73] Hence, the localized d-electrons of Fe and Co ions replace the cation sites of Ba^{2+} and

Ti^{4+} and the sp-d spin-exchange interaction between the band of electron orbitals. The lowest value of band gap energy was mainly observed for BCTF with the substitutions of Co^{2+} in Ba^{2+} site and Fe^{3+} in Ti^{4+} site, which could result in an improvement of the surface area-to-volume ratio, a decrease in the average crystallite size, and Co clustering. Besides, the optical band gap energy may be affected by several factors, including defects in the microstructure of the compounds, the grain size, and the chemical structure.[74,75] Furthermore, the diminution in the optical band gap energy with the decreasing grain size from 8.7 to 5.9 5.9 μm may be due to three different factors, including Columbian interactions, oxygen defects, and the competing microstrain effects. Moreover, the use of metal transition ions for doping, such as co-doping with Fe and Co, is a productive technique to create visible-light-driven photocatalysts. Indeed, impurity levels create forbidden bands that can cause the acceptor level to move below the original conduction band or the donor level to move above the original valence band, both of which lead to a narrowing of the optical band gap energy, and the creation of oxygen vacancies also plays an important role in narrowing the band gap.[4] According to our results, the presence of Fe and Co dopants enhances absorption in the BTO ceramic. The BTO ceramic exhibits a photoresponse in both visible light and ultraviolet spectra. Thus, it has a greater potential for photocatalysis in UV and visible light.

3.7. Thermal Conductivity Study. Table 3 summarizes the thermal conductivity values of the BTO, BFTC, and BCTF

Table 3. Thermal Conductivity of BTO, BFTC, and BCTF Samples

sample	thermal conductivity W m^{-1} K^{-1}	
	RT	180 °C
BTO	2.23	2.02
BFTC	0.91	0.34
BCTF	0.76	0.27

ceramic samples measured at different temperatures. The value of thermal conductivity of the BTO ceramic prepared by the sol−gel method is 2.23 W m^{-1} K^{-1} at ambient temperature, which is exactly in the range of values reported for the same material with different processing methods.[35,76−78] Several factors can describe the changes in the thermal conductivity behavior. These include the amount and type of substitution in a given material, different manufacturing techniques used to produce ceramic materials, and different measurement techniques. To estimate the overall thermal conductivity, the electrical thermal conductivity and the lattice thermal conductivity are typically combined. Furthermore, the thermal conductivity of ceramic materials in powder form is significantly lower than those in compact form, to a certain extent. The heat-transfer performance of the powders is strongly influenced by the interface, porosity, contacts, particle composition, and packing density. The determined value of thermal conductivity of BTO ceramics decreases by almost 66% of its original value after co-doping at room temperature and further decreases with increasing temperature by 86% of the first measured value (from 2.02 W m^{-1} K^{-1} for BTO to 0.27 W m^{-1} K^{-1} for BCTF). The observed changes in the behavior of the thermal conductivity results are attributed to the variation of the strength of the bonds along the atoms.[79] Besides, anharmonic scattering plays an important role in the

variation of thermal conductivity as a function of temperature. Indeed, at room temperature, the Fe- and Co-modified BT samples exhibit a regular decrease in thermal conductivity with doping, which continues decreasing with increasing temperature, indicating that a phonon−phonon defect[80] prevails in the studied temperature range. Co and Fe co-doped materials indeed have lower thermal conductivities which are less temperature-dependent. This is favored by a relative increase in the temperature independence of the phonon−defect interaction. For the BTO, BFTC, and BCTF samples, the thermal conductivity is distributed in the same order as the lattice parameters: BCTF < BFTC < BTO. Muta et al.[81] have observed that the difference in mass and ionic radius between the dopants and the matrix of a given perovskite material is proportional to the relaxation time of the phonon−defect interaction. For example, Co^{2+} and Fe^{3+} ions have a lower atomic mass than Ti and a smaller ionic radius than Ba^{2+},[82] indicating that the phonon−defect interaction is not generated by the mass difference but mainly by the lattice distortion due to the different ionic radii of Co^{2+}, Fe^{3+}, Ba^{2+}, and Ti^{4+}. Consequently, the thermal conductivity reaches its lowest value when the ionic radius is smaller. The ionic radii of Fe^{2+} and Co^{2+} ions are smaller than the ionic radii of Ba^{2+} (1.61 Å) and Ti^{4+} (0.60 Å), resulting in a decrease in thermal conductivity as the lattice system becomes highly distorted. The resulting lattice distortion may not be induced indefinitely while maintaining the lattice structure, resulting in a lower thermal conductivity limit as is the case of BFTC and BCTF co-doped materials. The failure of the thermal phonons in the band gap range inevitably leads to a decrease in thermal conductivity. Therefore, when the band gap is lower, the reduced thermal conductivity is higher, and the thermal conductivity is lower. Moreover, the oxygen vacancies generated in the doped samples have a significant contribution to the reduction in thermal conductivity. As shown in Table 3, the samples with low thermal conductivity values were the ceramics substituted by Fe and Co elements. Furthermore, the microstructure of the studied fractured ceramics displayed a distribution of small microscopic pores in the SEM microphotographs (Figure 7). The more complex the surface of the particles, the lower is the thermal conductivity. Large micropores are found in all samples, resulting in low thermal conductivity.

3.8. Mechanical Investigation. Table 4 presents the Young's modulus and compressive strength of the BTO,

Table 4. Compressive Strength and Young's Modulus of BTO, BFTC, and BCTF Ceramic Pellets

sample	mechanical properties	
	compressive strength (MPa)	Young's modulus
BTO	32.91	188.28
BFTC	27.25	183.26
BCTF	26.81	177.37

BFTC, and BCTF ceramics measured at room temperature. The compressive strength of the ceramic specimens was 32.91, 27.25, and 26.81 MPa for BTO, BFTC, and BCTF, respectively. However, the compressive strength measurements under Fe and Co co-doping did not show significant differences. In addition to the microstructure and grain size distribution, the cohesive forces within the grains of the ceramic pellets are mainly influenced by particle separation,

pores, and shrinkage. Hussein et al.[83] found that the largest value for compressive strength was mainly found for the irregularly distributed grains. In this study, the BTO ceramic pellet exhibited a higher compressive strength value (32.91 MPa) due to the microstructure and morphology of BTO which primarily contains irregularly oriented flat block grains; this fact contributes significantly to the weakening of the bond between atoms. As shown by the SEM analysis, the microstructures of BTO, BFTC, and BCTF differ massively from each other. In the case of BCTF (5.9 μm average grain size) which contains flat block shapes, the pores are almost identical in shape and size to that of the studied grains and arein the shape of flat blocks in both cases. Additionally, the pores in BTO, which have a larger grain size, are also larger and have a flat block shape appearance. For the BTO ceramic material with a larger grain size, the highest value for compressive strength was obtained, while for the BCTF ceramic compound with the smallest grain size, the lowest value was 26.81 MPa.

4. CONCLUSIONS

In this study, ceramic compounds $BaTiO_3$ (BTO), $(Ba_{0.97}Fe_{0.03})(Ti_{0.97}Co_{0.03})O_3$ (BFTC), and $(Ba_{0.97}Co_{0.03})(Ti_{0.97}Fe_{0.03})O_3$ (BCTF) have been successfully produced by the wet sol−gel method. The effect of co-doping BTO with Co and Fe is studied in detail and compared with the BTO compounds in terms of structural, microstructural, optical, temperature-dependent thermal conductivity, and mechanical properties. The tetragonal single-phase structures of BTO, BFTC, and BCTF ceramic compounds were developed at a temperature of 980 °C. The calculated values increase when Ba^{2+} is substituted by Co^{2+} and Ti^{4+} is replaced by Fe^{3+}, which is attributed to the variation of shrinkage of the system. The distortion in the tetragonal structure of the perovskite ferroelectrics is confirmed by the calculated value of the tolerance factor, which is 1.058 for BTO and 1.07 for BCTF. The SEM examination has shown the formation of flat block particles with a tendency to grain size reduction in Fe and Co doping. An increase in the spacing within the Ti−O bonds and a change in bond strength may be responsible for the decrease in thermal conductivity as a function of Co and Fe doping. Anharmonic scattering has been shown to play an important role in changing temperature-dependent thermal conductivity. The thermal conductivity of BFTC and BCTF samples decreases continuously with doping at room temperature and at a higher temperature, which shows that phonon−phonon scattering predominates at the considered temperature. Moreover, Co and Fe co-doped materials have lower and less temperature-dependent thermal conductivity. This is related to the temperature-independent relative increase in phonon−impurity scattering. To the best of our best knowledge, such an observation has not previously been reported for such materials. The band gap energy of the ceramics has been significantly reduced due to the creation of oxygen vacancies and the introduction of lattice distortions. The mechanical strength study has shown that the compressive strength of the BTO, BFTC, and BCTF ceramics decreases with the incorporation of Fe and Co dopants in Ba and Ti sites, which is assigned to the morphology and grain size distribution of the samples. The highest compressive strength was observed for the BTO ceramics proving that the compressive strength of the manufactured ceramic compounds is influenced by microstructural features. The developed materials can be used as versatile smart materials in micro-optical−electromechanical systems by combining their remarkable thermal and optical properties.

■ AUTHOR INFORMATION

Corresponding Author

Jamal Eldin F. M. Ibrahim − *Department of Materials Technology, University of Bahri, Khartoum 12217, Sudan*; Email: jamalfadoul@gmail.com

Authors

Mohammed Tihtih − *Institute of Ceramics and Polymer Engineering, University of Miskolc, Miskolc H-3515, Hungary*; ⊙ orcid.org/0000-0001-7364-9036

Mohamed A. Basyooni − *Department of Nanotechnology and Advanced Materials, Graduate School of Applied and Natural Science, Selçuk University, Konya 42030, Türkiye; Science and Technology Research and Application Center (BITAM), Necmettin Erbakan University, Konya 42090, Türkiye*; ⊙ orcid.org/0000-0001-8473-8253

Redouane En-nadir − *LPS, FSDM, Sidi Mohammed Ben Abdellah University, Fes 30000, Morocco*

Irina Hussainova − *Department of Mechanical and Industrial Engineering, Tallinn University of Technology, 19086 Tallinn, Estonia*

István Kocserha − *Institute of Ceramics and Polymer Engineering, University of Miskolc, Miskolc H-3515, Hungary*

Complete contact information is available at:
https://pubs.acs.org/10.1021/acsomega.2c07660

Notes

The authors declare no competing financial interest.

■ REFERENCES

(1) Kabra, H.; Deore, H. A.; Patil, P. Review on Advanced Piezoelectric Materials (BaTiO₃, PZT). *J. Emerg. Technol. Innov. Res.* **2019**, *6*, 950.

(2) Rathod, V. T. A Review of Acoustic Impedance Matching Techniques for Piezoelectric Sensors and Transducers. *Sensors* **2020**, *20*, 4051.

(3) Wang, D.; Chen, J. S. Progress on the Applications of Piezoelectric Materials in Sensors. *Mater. Sci. Forum* **2016**, *848*, 749−756.

(4) Tihtih, M.; Ibrahim, J.-E. F. M.; Basyooni, M. A.; Kurovics, E.; Belaid, W.; Hussainova, I.; Kocserha, I. Role of A-Site (Sr), B-Site (Y), and A, B Sites (Sr, Y) Substitution in Lead-Free BaTiO₃ Ceramic Compounds: Structural, Optical, Microstructure, Mechanical, and Thermal Conductivity Properties. *Ceram. Int.* **2022**, *49*, 1947−1959.

(5) Wang, W.; Jiang, Y.; Thomas, P. J. Structural Design and Physical Mechanism of Axial and Radial Sandwich Resonators with Piezoelectric Ceramics: A Review. *Sensors* **2021**, *21*, 1112.

(6) Ma, Y.; Song, J.; Wang, X.; Liu, Y.; Zhou, J. Synthesis, Microstructure and Properties of Magnetron Sputtered Lead Zirconate Titanate (PZT) Thin Film Coatings. *Coatings* **2021**, *11*, 944.

(7) Gupta, P.; Sen, S.*Structural, Optoelectronic and Ferroelectric Behavior of A & B Site Modified BaTiO3*; 2020, http://dspace.iiti.ac.in:8080/jspui/handle/123456789/2546.

(8) Vagadia, M.; Ravalia, A.; Solanki, P. S.; Pandey, P.; Asokan, K.; Kuberkar, D. G. Electrical Properties of BaTiO3 Based − MFIS

Heterostructure: Role of Semiconductor Channel Carrier Concentration. *AIP Adv.* **2014**, *4*, No. 057131.

(9) Hu, D.; Pan, Z.; Tan, X.; Yang, F.; Ding, J.; Zhang, X.; Li, P.; Liu, J.; Zhai, J.; Pan, H. Optimization the Energy Density and Efficiency of BaTiO3-Based Ceramics for Capacitor Applications. *Chem. Eng. J.* **2021**, *409*, No. 127375.

(10) Tihtih, M.; Ibrahim, J. E. F. M.; Basyooni, M. A.; Belaid, W.; Gömze, L. A.; Kocserha, I. Structural, Optical, and Electronic Properties of Barium Titanate: Experiment Characterisation and First-Principles Study. *Adv. Perform. Mater.* **2022**, *37*, 2995−3005.

(11) Tihtih, M.; Ibrahim, J. E. F. M.; Kurovics, E.; Gömze, L. A. Study of the Structure, Microstructure and Temperature Dependent Thermal Conductivity Properties of $SrTiO_3$: Via Y^{3+} Substitution. *J. Nano Res.* **2021**, *69*, 33−42.

(12) Tihtih, M.; Ibrahim, J. F. M.; Kurovics, E.; Abdelfattah, M. Study on the Effect of Bi Dopant on the Structural and Optical Properties of $BaTiO_3$ Nanoceramics Synthesized via Sol-Gel Method. *J. Phys.: Conf. Ser.* **2020**, *1527*, No. 012043.

(13) Goel, S.; Tyagi, A.; Garg, A.; Kumar, S.; Baskey, H. B.; Gupta, R. K.; Tyagi, S. Microwave Absorption Study of Composites Based on $CQD@BaTiO_3$ Core Shell and $BaFe_{12}O_{19}$ Nanoparticles. *J. Alloys Compd.* **2021**, *855*, No. 157411.

(14) Song, E.; Kim, D. H.; Jeong, E. J.; Choi, M.; Kim, Y.; Jung, H. J.; Choi, M. Y. Effects of Particle Size and Polymorph Type of TiO_2 on the Properties of BaTiO3 Nanopowder Prepared by Solid-State Reaction. *Environ. Res.* **2021**, *202*, No. 111668.

(15) Habib, M.; Munir, M.; Akram, F.; Lee, S.; Song, T. K.; Turak, A.; Kim, M. H.; Hussain, A. Structural Evolution and Electromechanical Properties of $SrTiO_3$-Modified $Bi_{0.5}Na_{0.5}TiO_3$−$BaTiO_3$ Ceramics Prepared by Sol-Gel and Hydrothermal Methods. *Mater. Chem. Phys.* **2021**, *266*, No. 124529.

(16) Tihtih, M.; Limame, K.; Ababou, Y.; Sayouri, S.; Ibrahim, J.-E. F. M. Sol-Gel Synthesis and Structural Characterization of Fe Doped Barium Titanate Nanoceramics. *Epitoanyag-Journal of Silicate Based and Composite Materials* **2019**, *71*, 190−193.

(17) Pradhan, D. K.; Mohanty, H. S.; Kumari, S.; Bhoi, K.; Tang, N.; Ravikant; Rahaman, M. M.; Pradhan, D. K.; Kumar, A.; Gilbert, D. A.; Rack, P. D. Ferroic Phase Transitions and Magnetoelectric Coupling in Cobalt Doped $BaTiO_3$. *J. Mater. Chem. C* **2021**, *12694*.

(18) Jain, A.; Panwar, A. K. Synergetic Effect of Rare-Earths Doping on the Microstructural and Electrical Properties of Sr and Ca Co-Doped $BaTiO_3$ Nanoparticles. *Ceram. Int.* **2020**, *46*, 10270−10278.

(19) Chen, L.; Fu, Q.; Jiang, Z.; Xing, J.; Gu, Y.; Zhang, F.; Jiang, Y.; Gu, H. Cathodoluminescence Evaluation of the Degradation of Mg, Ca and Dy Co-Doped $BaTiO_3$ Ceramics. *J. Eur. Ceram. Soc.* **2021**, *7654*.

(20) Chen, L.; Wang, H.; Zhao, P.; Shen, Z.; Zhu, C.; Cen, Z.; Li, L.; Wang, X. Effect of MnO_2 on the Dielectric Properties of Nb-Doped $BaTiO_3$-$(Bi_{0.5}Na_{0.5})TiO_3$ Ceramics for X9R MLCC Applications. *J. Am. Ceram. Soc.* **2019**, *102*, 2781−2790.

(21) Devmunde, B. H.; Somwanshi, S. B.; Kharat, P. B.; Solunke, M. B. Rare Earth Ion (La^{3+}) Doped $BaTiO_3$ Perovskite Nanoceramics for Spintronic Applications. *J. Phys.: Conf. Ser.* **2020**, *1644*, No. 012055.

(22) Staruch, M.; ElBidweihy, H.; Cain, M. G.; Thompson, P.; Lucas, C. A.; Finkel, P. Magnetic and Multiferroic Properties of Dilute Fe-Doped $BaTiO_3$ Crystals. *APL Mater.* **2020**, *8*, No. 031109.

(23) Rani, A.; Kolte, J.; Gopalan, P. Structural, Electrical, Magnetic and Magnetoelectric Properties of Co-Doped $BaTiO_3$ Multiferroic Ceramics. *Ceram. Int.* **2018**, *44*, 16703−16711.

(24) Pradhan, S.; Kaur, H.; Jayasimhadri, M. Photoluminescence and Thermal Sensing Properties of Er^{3+} Doped Silicate Based Phosphors for Multifunctional Optoelectronic Device Applications. *Ceram. Int.* **2021**, *47*, 27694−27701.

(25) Rani, A.; Kolte, J.; Vadla, S. S.; Gopalan, P. Structural, Electrical, Magnetic and Magnetoelectric Properties of Fe Doped $BaTiO_3$ Ceramics. *Ceram. Int.* **2016**, *42*, 8010−8016.

(26) Gouadria, H.; Smari, M.; Mnasri, T.; Necib, J.; López Sánchez, J.; Marín, P.; Jamale, A. P.; Ben Younes, R. Implementing a Sol-Gel Route to Adjust the Structural and Dielectric Characteristics of Bi and

(27) Singh, D.; Dixit, A.; Dobal, P. S.Ferroelectricity and Ferromagnetism in Fe-Doped Barium Titanate Ceramics. **2021**, *573* (1), 63−75. DOI: 10.1080/00150193.2021.1890464.

(28) Costanzo, T.; McCracken, J.; Rotaru, A.; Caruntu, G. Quasi-Monodisperse Transition-Metal-Doped $BaTiO_3$ (M = Cr, Mn, Fe, Co) Colloidal Nanocrystals with Multiferroic Properties. *ACS Appl. Nano Mater.* **2018**, *1*, 4863−4874.

(29) Fan, B.; Yang, G.; Li, M. Y.; Liu, P.; Qiu, S.; Shen, M.; Liu, H.; Zhang, G.; Wang, Q.; Jiang, S. Lead-Free $Ba_{(1-x)}Sr_xTiO_3$ Ceramics for Room-Temperature Pyroelectric Energy Conversion. *Ceram. Int.* **2018**, *44*, 8270−8276.

(30) Jiang, S.; Liu, P.; Zhang, X.; Zhang, L.; Li, Q.; Yao, J.; Zeng, Y.; Wang, Q.; Zhang, G. Enhanced Pyroelectric Properties of Porous $Ba_{0.67}Sr_{0.33}TiO_3$ Ceramics Fabricated with Carbon Nanotubes. *J. Alloys Compd.* **2015**, *636*, 93−96.

(31) Konysheva, E.; Irvine, J. T. S. In Situ High-Temperature Neutron Diffraction Study of A-Site Deficient Perovskites with Transition Metals on the B-Sublattice and Structure-Conductivity Correlation. *Chem. Mater.* **2011**, *23*, 1841−1850.

(32) Giordano, L.; Akkiraju, K.; Jacobs, R.; Vivona, D.; Morgan, D.; Shao-Horn, Y. Electronic Structure-Based Descriptors for Oxide Properties and Functions. *Acc. Chem. Res.* **2022**, *55*, 298−308.

(33) Alshoaibi, A.; Kanoun, M. B.; Ul Haq, B.; Alfaify, S.; Goumri-Said, S. Insights into the Impact of Yttrium Doping at the Ba and Ti Sites of BaTiO3on the Electronic Structures and Optical Properties: A First-Principles Study. *ACS Omega* **2020**, *5*, 15502−15509.

(34) Chen, J.; Deng, H.; Pan, Y.; Zheng, D.; Sun, L.; Tao, J.; Yang, P.; Chu, J. Band Gap Modulation and Improved Magnetism of Double Perovskite Sr_2KMoO_6 (K = Fe, Co, Ni, Mn) Doped $BaTiO_3$ Ceramics. *Ceram. Int.* **2022**, *48*, 7629−7635.

(35) Xing, J.; Radovic, M.; Muliana, A. Thermal Properties of $BaTiO_3$/Ag Composites at Different Temperatures. *Composites, Part B* **2016**, *90*, 287−301.

(36) Ryu, S.-S.; Kim, H.-T.; Kim, H. J.; Kim, S. Characterization of Mechanical Properties of BaTiO3 Ceramic with Different Types of Sintering Aid by Nanoindentation. *J. Ceram. Soc. Japan* **2009**, *117*, 811−814.

(37) Zhang, N.; Yao, Z.; Hao, H.; Cao, M.; Liu, H. Selectively Designed Fe Doping of Lead-Free $BaTiO_3$ Piezoceramics. *J. Mater. Sci.: Mater. Electron.* **2022**, *33*, 10154−10164.

(38) Ku Muhsen, K. N. D.; Osman, R. A. M.; Idris, M. S.; Muhammad Nadzri, N. I.; Ruiz León, D. A. Structural Analysis and Dielectric Properties of Oxygen Non-Stoichiometry 5% Fe-Doped BaTiO3 Ceramic. *Adv. Sci. Technol.* **2022**, *118*, 47−52.

(39) Zhao, Y.; Wang, Q.; Lv, J. H.; Zhao, X.; Wang, C. M. Dielectric Properties and Electrocaloric Effect of Yttrium-Modified $BaTiO_3$ Ceramics. *Ceram. Int.* **2021**, *47*, 18610−18618.

(40) Amaechi, I. C.; Hadj Youssef, A.; Kolhatkar, G.; Rawach, D.; Gomez-Yañez, C.; Claverie, J. P.; Sun, S.; Ruediger, A. Ultrafast Microwave-Assisted Hydrothermal Synthesis and Photocatalytic Behaviour of Ferroelectric Fe^{3+}-Doped $BaTiO_3$ Nanoparticles under Simulated Sunlight. *Catal. Today* **2021**, *360*, 90−98.

(41) Peng, W.; Li, L.; Yu, S.; Yang, P.; Xu, K. Dielectric Properties, Microstructure and Charge Compensation of MnO_2-Doped $BaTiO_3$-Based Ceramics in a Reducing Atmosphere. *Ceram. Int.* **2021**, *47*, 29191−29196.

(42) Rani, A.; Kolte, J.; Gopalan, P. Influence of Sintering Temperature on Structural, Electrical, and Magnetoelectric Properties of Multiferroic Fe-Substituted $BaTiO_3$ Ceramics. *Appl. Phys. A: Mater. Sci. Process.* **2022**, *128*, 442.

(43) Ryu, G. H.; Bowes, P. C.; McGarrahan, J. R.; Irving, D. L.; Dickey, E. C. Fermi Level Pinning in Co-Doped BaTiO3: Part I. DC and AC Electrical Conductivities and Degradation Behavior. *J. Am. Ceram. Soc.* **2022**, *105*, 292−298.

(44) Tihtih, M.; Ibrahim, J. E. F. M.; Kurovics, E.; Gömze, L. A. Synthesis of $Ba_{1-x}Sr_xTiO_3$ (x = 0−0.3) Ceramic Powders via Sol-Gel

Method: Structural, Microstructure, Thermal Conductivity, and Compressive Strength Properties. *Cryst. Res. Technol.* **2021**, 2100106.

(45) Tihtih, M.; Ponaryadov, A. A.; Ibrahim, J.-E. F. M.; Kurovics, E.; Kotova, E. L.; Gömze, L. A. Effect of Temperature on the Structural Properties of Barium Titanate Nanopowders Synthesis via Sol-Gel Process. *Epitoanyag-Journal of Silicate Based and Composite Materials* **2020**, *72*, 165−168.

(46) Moghtada, A.; Heidary Moghadam, A.; Ashiri, R. Tetragonality Enhancement in $BaTiO_3$ by Mechanical Activation of the Starting $BaCO_3$ and TiO_2 Powders: Characterization of the Contribution of the Mechanical Activation and Postmilling Calcination Phenomena. *Int. J. Appl. Ceram. Technol.* **2018**, *15*, 1518−1531.

(47) Yansen, W.; Kim, D.; Parwanta, K. J.; Liu, C.; Lee, B. W. Rietveld Analysis and Multiferroic Properties of Fe Doped $Ba_{0.95}Bi_{0.05}TiO_3$ Ceramics. *Curr. Appl. Phys.* **2015**, *15*, 120−123.

(48) Mansuri, A.; Bhatti, I. N.; Bhatti, I. N.; Mishra, A. Investigation of Structural Phase Evolution and Dielectric Response of Co-Doped $BaTiO_3$. *J. Adv. Dielectr.* **2018**, *08*, 1850024.

(49) Masó, N.; Beltrán, H.; Cordoncillo, E.; Escribano, P.; West, A. R. Electrical Properties of Fe-Doped $BaTiO_3$. *J. Mater. Chem.* **2006**, *16*, 1626−1633.

(50) Cullity, B. D. Elements of X-Ray Diffraction. *Am. J. Phys.* **1957**, *25*, 394.

(51) Rajan, S.; Gazzali, P. M. M.; Chandrasekaran, G. Electrical and Magnetic Phase Transition Studies of Fe and Mn Co-Doped $BaTiO_3$. *J. Alloys Compd.* **2016**, *656*, 98−109.

(52) Redhu, P.; Punia, R.; Hooda, A.; Malik, B. P.; Sharma, G.; Sharma, P. Correlation between Multifunctional Properties of Lead Free Iron Doped BCT Perovskite Ceramics. *Ceram. Int.* **2020**, *46*, 17495−17507.

(53) Freeman, C. L.; Dawson, J. A.; Chen, H. R.; Harding, J. H.; Ben, L.-B.; Sinclair, D. C. A New Potential Model for Barium Titanate and Its Implications for Rare-Earth Doping. *J. Mater. Chem.* **2011**, *21*, 4861−4868.

(54) Eichel, R. A. Defect Structure of Oxide Ferroelectrics-Valence State, Site of Incorporation, Mechanisms of Charge Compensation and Internal Bias Fields : IInvited Review for. *J. Electroceram.* **2007**, *19*, 9−21.

(55) Lee, S.; Woodford, W. H.; Randall, C. A. Crystal and Defect Chemistry Influences on Band Gap Trends in Alkaline Earth Perovskites. *Appl. Phys. Lett.* **2008**, *92*, No. 201909.

(56) Ferrari, M.; Lutterotti, L. Method for the Simultaneous Determination of Anisotropic Residual Stresses and Texture by X-ray Diffraction. *J. Appl. Phys.* **1998**, *76*, 7246.

(57) Sharma, P.; Kumar, P.; Kundu, R. S.; Juneja, J. K.; Ahlawat, N.; Punia, R. Structural and Dielectric Properties of Substituted Barium Titanate Ceramics for Capacitor Applications. *Ceram. Int.* **2015**, *41*, 13425−13432.

(58) Puli, V. S.; Li, P.; Adireddy, S.; Chrisey, D. B. Crystal Structure, Dielectric, Ferroelectric and Energy Storage Properties of La-Doped $BaTiO_3$ Semiconducting Ceramics. *J. Adv. Dielectr.* **2015**, *05*, No. 1550027.

(59) Singh, M.; Yadav, B. C.; Ranjan, A.; Kaur, M.; Gupta, S. K. Synthesis and Characterization of Perovskite Barium Titanate Thin Film and Its Application as LPG Sensor. *Sens. Actuators, B* **2017**, *241*, 1170−1178.

(60) Venkateswaran, U. D.; Naik, V. M.; Naik, R. High-Pressure Raman Studies of Polycrystalline. *Phys. Rev. B: Condens. Matter Mater. Phys.* **1998**, *58*, 14256−14260.

(61) Soni, M.; Saleem, M.; Bajpai, N.; Chouhan, S.; Varshney, M. D.; Mishra, A. Structural and Optical Properties on Na Doped $BaTiO_3$. *AIP Conf. Proc.* **2019**, *2100*, No. 020185.

(62) Choi, G.; Choi, A. H.; Evans, L. A.; Akyol, S.; Ben-Nissan, B. A Review: Recent Advances in Sol-gel-derived Hydroxyapatite Nanocoatings for Clinical Applications. *J. Am. Ceram. Soc.* **2020**, *103*, 5442−5453.

(63) Ganguly, M.; Rout, S. K.; Ahn, C. W.; Kim, I. W.; Kar, M. Structural, Electrical and Optical Properties of $Ba(Ti_{1-x}Yb_{4x/3})O_3$ Ceramics. *Ceram. Int.* **2013**, *39*, 9511−9524.

(64) Khirade, P. P.; Vinayak, V.; Kharat, P. B.; Chavan, A. R. Green Synthesis of $Ba_{1-x}Sr_xTiO_3$ Ceramic Nanopowders by Sol-Gel Combustion Method Using Lemon Juice as a Fuel: Tailoring of Microstructure, Ferroelectric, Dielectric and Electrical Properties. *Opt. Mater.* **2021**, *111*, No. 110664.

(65) Souza, A. E.; Santos, G. T. A.; Barra, B. C.; MacEdo, W. D.; Teixeira, S. R.; Santos, C. M.; Senos, A. M. O. R.; Amaral, L.; Longo, E. Photoluminescence of $SrTiO_3$: Influence of Particle Size and Morphology. *Cryst. Growth Des.* **2012**, *12*, 5671−5679.

(66) Suwannaruang, T.; Kidkhunthod, P.; Butburee, T.; Shivaraju, H. P.; Shahmoradi, B.; Wantala, K. Facile Synthesis of Cooperative Mesoporous-Assembled CexSr1-XFexTi1-XO3 Perovskite Catalysts for Enhancement Beta-Lactam Antibiotic Photodegradation under Visible Light Irradiation. *Surf. Interfaces* **2021**, *23*, No. 101013.

(67) Niesz, K.; Ould-Ely, T.; Tsukamoto, H.; Morse, D. E. Engineering Grain Size and Electrical Properties of Donor-Doped Barium Titanate Ceramics. *Ceram. Int.* **2011**, *37*, 303−311.

(68) Jo, S. K.; Park, J. S.; Han, Y. H. Effects of Multi-Doping of Rare-Earth Oxides on the Microstructure and Dielectric Properties of $BaTiO_3$. *J. Alloys Compd.* **2010**, *501*, 259−264.

(69) Myrick, M. L.; Simcock, M. N.; Baranowski, M.; Brooke, H.; Morgan, S. L.; McCutcheon, J. N.The Kubelka-Munk Diffuse Reflectance Formula Revisited. **2011**, *46* (2), 140−165, DOI: 10.1080/05704928.2010.537004.

(70) Manzoor, S.; Husain, S. Analysis of Zn Substitution on Structure, Optical Absorption, Magnetization, and High Temperature Specific Heat Anomaly of the Nano-Crystalline $LaFeO_3$. *J. Appl. Phys.* **2018**, *124*, No. 065110.

(71) Xie, P.; Yang, F.; Li, R.; Ai, C.; Lin, C.; Lin, S. Improving Hydrogen Evolution Activity of Perovskite $BaTiO_3$ with Mo Doping: Experiments and First-Principles Analysis. *Int. J. Hydrogen Energy* **2019**, *44*, 11695−11704.

(72) Chandra Sati, P.; Arora, M.; Chauhan, S.; Kumar, M.; Chhoker, S. Effect of Dy Substitution on Structural, Magnetic and Optical Properties of $BiFeO_3$ Ceramics. *J. Phys. Chem. Solids* **2014**, *75*, 105−108.

(73) Kouotou, P. M.; El Kasmi, A.; Wu, L. N.; Waqas, M.; Tian, Z. Y. Particle Size-Band Gap Energy-Catalytic Properties Relationship of PSE-CVD-Derived Fe_3O_4 Thin Films. *J. Taiwan Inst. Chem. Eng.* **2018**, *93*, 427−435.

(74) Wu, P.; Pan, J.; Chen, X. Enhanced Visible-Light Absorption and Room-Temperature Ferromagnetism of $[KNbO_3]_{1-x}[BaFe_{1/2}Nb_{1/2}O_3\text{-}\delta]_x$ Solid Solutions. *J. Mater. Sci.: Mater. Electron.* **2022**, *33*, 690−702.

(75) Zheng, X.; Mofarah, S. S.; Cazorla, C.; Daiyan, R.; Esmailpour, A. A.; Scott, J.; Yao, Y.; Lim, S.; Wong, V.; Chen, E. Y.; Arandiyan, H.; Koshy, P.; Sorrell, C. C. Decoupling the Impacts of Engineering Defects and Band Gap Alignment Mechanism on the Catalytic Performance of Holey 2D CeO_{2-x}-Based Heterojunctions. *Adv. Funct. Mater.* **2021**, *31*, No. 2103171.

(76) Suchanicz, J.; Czaja, P.; Kluczewska, K.; Czternastek, H.; Sokolowski, M.; Węgrzyn, A. The Influence of $Pb(Mg_{1/3}Nb_{2/3})O_3$-Doping on the Thermoelectric Properties of BaTiO3 Ceramics. *Phase Transitions* **2018**, *91*, 1036−1043.

(77) Khan, T. T.; Ur, S. C. Thermoelectric Properties of the Yttrium-Doped Ceramic Oxide SrTiO3. *J. Korean Phys. Soc.* **2017**, *70*, 93−97.

(78) He, Y. Heat Capacity, Thermal Conductivity, and Thermal Expansion of Barium Titanate-Based Ceramics. *Thermochim. Acta* **2004**, *419*, 135−141.

(79) Muta, H.; Kurosaki, K.; Yamanaka, S. Thermoelectric Properties of Doped $BaTiO_3$-$SrTiO_3$ Solid Solution. *J. Alloys Compd.* **2004**, *368*, 22−24.

(80) Sun, Q.; Chen, S.-E.; Gao, Q.; Zhang, W.; Geng, J.; Zhang, Y. Analyses Of The Factors Influencing Sandstone Thermal Conductivity. *Acta Geodyn. Geomater.* **2017**, *14*, 173−180.

(81) Muta, H.; Kurosaki, K.; Yamanaka, S. Thermoelectric Properties of Rare Earth Doped SrTiO3. *J. Alloys Compd.* **2003**, *350*, 292−295.

(82) Liu, J.; Wang, C. L.; Li, Y.; Su, W. B.; Zhu, Y. H.; Li, J. C.; Mei, L. M. Influence of Rare Earth Doping on Thermoelectric Properties of SrTiO3 Ceramics. *J. Appl. Phys.* **2013**, *114*, No. 223714.

(83) Hussein, A. I.; Mat, A. N. C.; Abd Wahab, N. A. A.; Ab. Rahman, I.; Husein, A.; Ab-Ghani, Z. Synthesis and Properties of Novel Calcia-Stabilized Zirconia (Ca-SZ) with Nano Calcium Oxide Derived from Cockle Shells and Commercial Source for Dental Application. *Appl. Sci.* **2020**, *10*, 5751.